# Small Co-doping induced magnetic and electrical transitions in single crystal $CaFe_{0.95}Co_{0.05}O_3$

Hailiang Xia,[1] Zhehong Liu,[1,2] Yan Wu,[3] Qian Sun,[1] Naoaki Hayashi,[4] Xi Shen,[1,2] Huibo Cao,[3] Clarina dela Cruz,[3] Richeng Yu,[1,2] Yi-feng Yang,[1,2,*] Mikio Takano,[4] and Youwen Long[1,2,†]

[1]*Beijing National Laboratory for Condensed Matter Physics, Institute of Physics, Chinese Academy of Sciences, Beijing 100190, China*
[2]*School of Physics, University of Chinese Academy of Sciences, Beijing 100049, China*
[3]*Neutron Scattering Division, Oak Ridge National Laboratory, Oak Ridge, Tennessee 37831, USA*
[4]*Research Institute for Production Development, 15 Shimogamo-Morimoto, Sakyo, Kyoto 606–0805, Japan*

(Received 25 January 2026; revised 19 April 2026; accepted 20 May 2026; published 18 June 2026)

$CaFeO_3$ and $CaFe_{0.95}Co_{0.05}O_3$ single crystals were grown by combing floating-zone method with high oxygen pressure treatment. Both crystals show charge disproportionation of Fe ($Fe^{4+} \rightarrow Fe^{3+} + Fe^{5+}$) accompanied by a metal-to-insulator transition as well as a crystal structural transformation from *Pbnm* to $P2_1/n$. However, the slight introduction of Co significantly suppresses the critical temperature of charge disproportionation from 290 K in $CaFeO_3$ to 260 K in $CaFe_{0.95}Co_{0.05}O_3$. Different from the single antiferromagnetic phase transition as observed in the polycrystalline $CaFeO_3$, two sequential antiferromagnetic transitions are found to occur in these two single crystals with the Néel temperatures around 119 and 112 K for $CaFeO_3$ crystal and 109 and 98 K for $CaFe_{0.95}Co_{0.05}O_3$ crystal, respectively. Neutron diffraction illustrates the formation of a spiral antiferromagnetic structure. Moreover, as the temperature further decreases to 65 K, a third magnetic transition accompanied by a second electrical transition is observed in the slightly Co-doped $CaFe_{0.95}Co_{0.05}O_3$ crystal. First-principles calculations suggest that the introduction of a moderate amount of Co and the peculiar spiral spin texture play an important role in the presence of such new magnetic and electrical transitions.

DOI: 10.1103/lssr-fzlr

## I. INTRODUCTION

The perovskite oxides of $AFeO_3$ ($A$ = Ca, Sr, Ba) have received much attention due to their intriguing structural, magnetic, and electrical properties [1–5]. For example, $SrFeO_3$ exhibits versatile helimagnetic phases under different magnetic fields [2], while $BaFeO_3$ undergoes multiple magnetic and electrical transitions at different temperatures [3]. $CaFeO_3$ is particularly notable for its charge disproportionation (CD) behavior. Specifically, as the temperature decreases to about 290 K, the uniform tetravalent $Fe^{4+}(d^5\underline{L})$ state of $CaFeO_3$ transforms into charge-disproportionated $Fe^{3+}(d^5)$ and $Fe^{5+}(d^5\underline{L}^2)$ states, where $\underline{L}$ represents a ligand hole from the O-2$p$ bands due to the considerable negative $p-d$ charge transfer energy [1,6]. The CD leads to a structural transition from an orthorhombic *Pbnm* phase with a single $Fe^{4+}$ Wyckoff site to a monoclinic $P2_1/n$ phase with two distinct $Fe^{3+}$ and $Fe^{5+}$ sites distributed in a rocksalt-type fashion. Moreover, the CD variation is accompanied by a metal-to-insulator transition. The formation of the $P2_1/n$ phase as well as the insulating transition in turn can be regarded as the hallmarks for the occurrence of CD in $CaFeO_3$. In addition, different B-site chemical doping has been studied for $CaFeO_3$. For example, the Co doping systematically modulates the CD and electronic properties [7]. The Zr doping has been shown to enhance the CD [8]. The Cu-doped $CaFeO_3$ demonstrates enhanced oxygen reduction reaction activity in electrocatalysis, making it an efficient cathode catalyst for microbial fuel cells [9]. Furthermore, the Mo-doped $CaFeO_3$ synthesized via hydrothermal routes has exhibited remarkable supercapacitor performance [10]. These results reveal that the B-site substitution in $CaFeO_3$ provides an intriguing method to tailor electronic structures and versatile physical properties.

Although higher-Co-doped $CaFe_{1-x}Co_xO_3$ samples with $x \geqslant 0.1$ have been studied in polycrystalline form [11], the lower-doping regime with $x < 0.1$, where subtle magnetic and electrical interactions may emerge, remains unexplored, especially in single-crystal form. The growth of such single crystals is challenging due to the high pressure required to stabilize the $Fe^{4+}/Co^{4+}$ valence states. Although previous attempts have been made [12], a detailed characterization of high-quality single crystals is lacking. Motivated by the unique CD of $CaFeO_3$ and the dramatic changes in magnetic and electrical properties induced by Co doping, as observed in its analogous $SrFeO_3$ and $BaFeO_3$ single crystals [13,14], this study focuses on the investigation of sizeable $CaFeO_3$ and $CaFe_{0.95}Co_{0.05}O_3$ single crystals. As expected, a CD-induced metal-to-insulator transition was observed in the parent $CaFeO_3$ crystal. Intriguingly, in contrast to reports on polycrystalline samples, which show a single antiferromagnetic (AFM) phase transition [11,15,16], the $CaFeO_3$ single crystal exhibits two successive magnetic transitions. Furthermore, introducing only 5% Co not only significantly suppresses the critical temperature of CD ($T_{CD}$) but also induces a third AFM transition. Most remarkably, this new magnetic transition is accompanied by a reentrant-like metallization transition with a drastic decrease in resistivity,

*Contact author: yifeng@iphy.ac.cn
†Contact author: ywlong@iphy.ac.cn

 

while the CD state remains robust. Thus, $CaFe_{0.95}Co_{0.05}O_3$ single crystal presents an interesting platform for exploring novel electronic states through slight chemical doping.

## II. EXPERIMENTAL AND CALCULATION METHODS

$CaFeO_3$ and $CaFe_{0.95}Co_{0.05}O_3$ single crystals with a diameter and height of 3.0–4.0 mm were grown by a two-step method [4,17]. First, oxygen-deficient precursor single crystals of $CaFe_{1-x}Co_xO_{2.5}$ ($x = 0$, 0.05) with a brownmillerite structure were prepared by floating-zone methods, and then the precursors were treated using a cubic anvil-type high-pressure apparatus at 6.0 GPa and 1073 K for 30 min with excess $KClO_4$ as the oxidizing source. X-ray Laue diffraction and powder X-ray diffraction (XRD) measurements were conducted using a Huber diffractometer (Cu$-K\alpha_1$ radiation, 40 kV, 300 mA). Thermogravimetric (TG) measurements were performed on a Setaram TG-DTA system with a temperature scan up to 1000 K under $N_2$ gas flow. The chemical homogeneity of the Co-doped crystal was examined by energy-dispersive X-ray spectroscopy (EDS) mapping using an ARM200F scanning transmission electron microscope equipped with a CEOS probe and image aberration correctors (JEOL). Magnetic susceptibility and magnetization were measured using a Quantum Design vibrating sample magnetometer. Resistivity and heat capacity data were collected using a Quantum Design physical property measurement system. The standard four-probe method was used for resistivity measurements with a sample size of approximately $1.0 \times 1.0 \times 1.5\text{mm}^3$. $^{57}$Fe Mössbauer spectra were acquired in transmission geometry on powder samples using a $^{57}$Co/Rh $\gamma$-ray source. The source velocity was calibrated by using pure $\alpha$-Fe. Single-crystal neutron diffraction experiments were performed on an HB-3A four-circle diffractometer at the High Flux Isotope Reactor (HFIR), Oak Ridge National Laboratory (ORNL). A 20 mg single crystal was used for the measurement with a neutron wavelength of 1.546 Å from a bent Si-220 monochromator [18]. Powder neutron diffraction was performed on the HB-2A powder diffractometer at HFIR, ORNL. A powder sample (1 g) was used for measurement at a neutron wavelength of 1.54 Å, which was selected by the vertically focusing Ge(115) monochromator. The crystal structure and magnetic structure refinements were performed using FULLPROF Suite [19].

First-principles calculations were performed using the full-potential linearized augmented plane-wave method and generalized-gradient approximation (GGA) with the Perdew-Burke-Ernzerhof exchange-correlation energy $U$ as implemented in the WIEN2K package [20]. In the GGA+$U$ calculations, we took $U$= 5 eV for Fe and 3 eV for Co in the presented results [21,22]. Other reasonable values of $U$ in proximity to the aforementioned selected values were also tested (see Supplemental Material Figure S1 [23]), but the main conclusions were not qualitatively affected. The muffin-tin radii were set as 2.00 a.u. for Ca, 1.60 a.u. for O, and 1.90 a.u. for Co and Fe. The maximum modulus for the reciprocal vectors was selected such that $R_{MT} \times K_{max} = 8.0$. We chose 1000 k-point meshes for the entire Brillouin zone. The low-temperature crystal structures were obtained using neutron powder diffraction. For low Co concentrations ($x = 0$ and 1/12), we used the $P2_1/n$ symmetry group with optimized lattice parameters of $a = 10.038$ Å, $b = 10.106$ Å, $c = 14.212$ Å.

TABLE I. Refinement structure parameters of $CaFeO_3$ and $CaFe_{0.95}Co_{0.05}O_3$ obtained at room temperature from x-ray diffraction. Space group: *Pbnm*, atomic positions: Ca 4*c* ($x$, $y$, 0.25), Fe/Co 4*b* (0, 0.5, 0), $O_1$ 8*d* ($x$, $y$, $z$), and $O_2$ 4*c* ($x$, $y$, 0.25).

| Parameters | $CaFeO_3$ | $CaFe_{0.95}Co_{0.05}O_3$ |
|---|---|---|
| a (Å) | 5.32609 (6) | 5.32615(5) |
| b (Å) | 5.35358 (8) | 5.35344(6) |
| c (Å) | 7.5396 (1) | 7.53948(8) |
| Ca (x) | 0.992(1) | 0.9877(5) |
| Ca (y) | 0.0329(3) | 0.0337(3) |
| O1 (x) | 0.713(1) | 0.716(1) |
| O1 (y) | 0.282(1) | 0.2889(9) |
| O1 (z) | 0.0289(8) | 0.0300(7) |
| O2 (x) | 0.067(2) | 0.059(1) |
| O2 (y) | 0.496(1) | 0.4912(9) |
| Fe(Fe/Co)-O1 (×2) (Å) | 1.937(6) Å | 1.903(6) Å |
| Fe(Fe/Co)-O1 (×2) (Å) | 1.900(7) Å | 1.940(6) Å |
| Fe(Fe/Co)-O2 (×2) (Å) | 1.918(2) Å | 1.9115(9)Å |
| ∠Fe(Fe/Co)-O1-Fe(Fe/Co) (deg) | 159.5(2) | 158.6(2)° |
| ∠Fe(Fe/Co)-O2-Fe(Fe/Co) (deg) | 158.5(5) | 160.8(3)° |
| $R_{wp}$ (%) | 1.41 | 1.40 |
| $R_p$ (%) | 1.13 | 1.09 |

## III. RESULTS AND DISCUSSION

Figures 1(a) and 1(b) show the powder XRD patterns acquired at room temperature for pulverized $CaFeO_3$ and $CaFe_{0.95}Co_{0.05}O_3$ single crystals, respectively. Rietveld refinements reveal that these two oxides crystallize into a $GdFeO_3$-type perovskite structure with the space group *Pbnm*, as identified in the parent polycrystalline sample [1]. The refined structural parameters are listed in Table I. Figure 1(c) presents the Laue diffraction results for $CaFeO_3$ and $CaFe_{0.95}Co_{0.05}O_3$ single crystals. The bright diffraction spots indicate the successful growth of single crystals for these two compounds. However, when a specific plane determined by Laue diffraction was cut to record the XRD pattern, two separate diffraction peaks were observed. For example, as shown in Fig. 1(d), both the (022) and (202) peaks were observed during the measurement of the (101) plane. These results reveal that crystal twins exist because of the similar *a*- and *b*-axis lattice parameters of these two orthorhombic perovskites (see Table I). Thus, a random plane was selected to measure the physical properties, as described later. TG measurements were conducted to determine the oxygen content. For instance, Fig. 1(e) shows the TG result of the $CaFeO_3$ crystal. The slight weight decrease below 400 K may be attributed to the loss of oxygen on the sample surface because of the use of excess oxidizing agent during the synthesis. The release of oxygen starts at approximately 600 K, whereupon the weight becomes almost constant above 800 K. Based on the TG loss between 400 and 1000 K, as well as the final product ($CaFeO_{2.5}$) that was identified by XRD, the oxygen

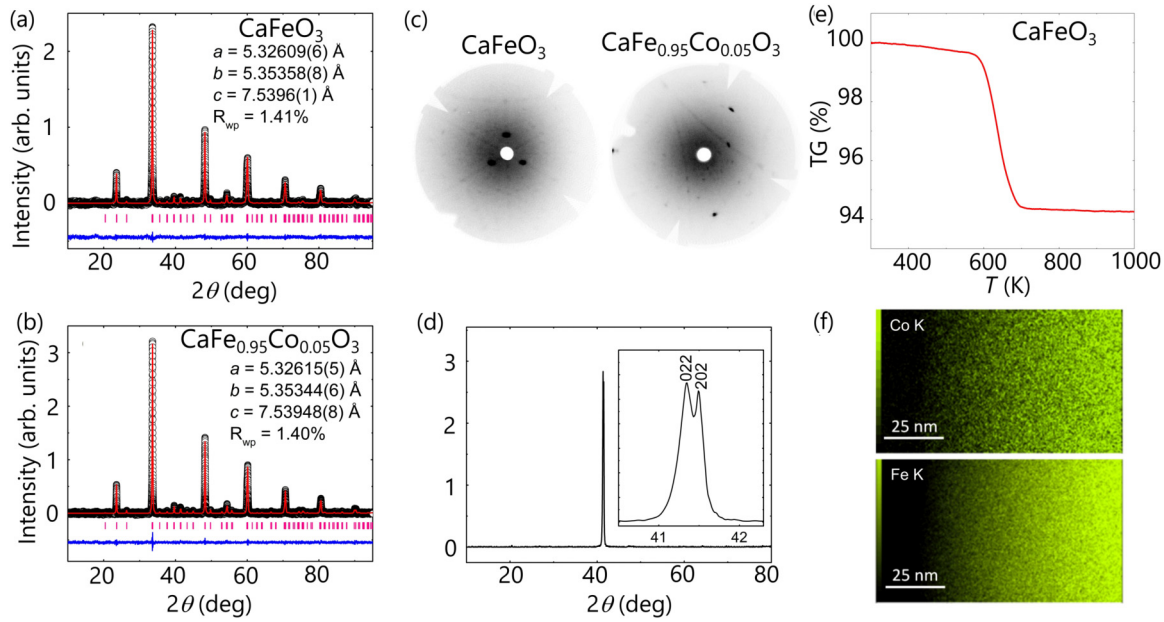


FIG. 1. Structure characterization and thermogravimetric analysis for $CaFeO_3$ and $CaFe_{0.95}Co_{0.05}O_3$ single crystals. (a), (b) Powder XRD patterns and the Rietveld refinement profiles of pulverized crystals of $CaFeO_3$ and $CaFe_{0.95}Co_{0.05}O_3$, respectively. The observed (circles), calculated (blue line), and difference (olive line) patterns are shown. The ticks show the positions of the Bragg reflections with space group *Pbnm*. (c) Representative Laue diffraction patterns of $CaFeO_3$ (left) and $CaFe_{0.95}Co_{0.05}O_3$ (right) single crystals. (d) XRD pattern of $CaFeO_3$ single crystal for the (110) plane. The insert shows the enlarged view of the two separated peaks. (e) Temperature dependence of TG loss for $CaFeO_3$. (f) Energy-dispersive X-ray spectroscopy mapping of $CaFe_{0.95}Co_{0.05}O_3$ single crystal collected along the [0- 21] zone-axis.

content of the $CaFeO_3$ crystal was determined to be 2.99(2). A similar TG result was obtained for the $CaFe_{0.95}Co_{0.05}O_3$ crystal, suggesting stoichiometric oxygen composition and the formation of the $Fe^{4+}/Co^{4+}$ state. Furthermore, to clarify the elemental distribution of the Fe and Co ions at the B-site in the doped $CaFe_{0.95}Co_{0.05}O_3$ crystal, EDS mapping was performed along the [0- 21] zone-axis. As depicted in Fig. 1(f), there were no discernible Fe- and Co-rich zones, indicating the homogeneous substitution of Fe by Co.

Figures 2(a) and 2(b) show the temperature dependence of the magnetic susceptibility ($\chi$) and specific heat ($C_P$) of the $CaFeO_3$ and $CaFe_{0.95}Co_{0.05}O_3$ crystals, respectively. Although only a single AFM phase transition was observed in polycrystalline $CaFeO_3$ [11], in the related single crystal grown in this work, both the $\chi$ and $C_P$ curves display two clear anomalies at $T_{N1} \approx 119$ K and $T_{N2} \approx 112$ K, illustrating the occurrence of double second-order AFM phase transitions without thermal hysteresis. When $CaFeO_3$ was doped with Co to partly replace Fe, the AFM Néel temperatures changed significantly. As shown in Fig. 2(b), Co-doping of only 5% lowers $T_{N1}$ to 109 K and $T_{N2}$ to 98 K. Unexpectedly, decreasing the temperature to $T_{N3} \approx 65$ K leads to the observation of a newly presented third AFM-like phase transition in the $CaFe_{0.95}Co_{0.05}O_3$ crystal. Moreover, the zero-field-cooling (ZFC) and field-cooling (FC) susceptibility curves displayed thermal hysteresis around $T_{N3}$ (refer to the inset of Fig. 2(b) for clarity), reflecting the different nature of this emerging magnetic transition from those occurring at $T_{N1}$ and $T_{N2}$. This value of $T_{N3}$ was determined based on the FC curve during cooling. As expected from the paramagnetism above $T_{N1}$ or long-range AFM ordering at lower temperatures, linear magnetization behaviors were observed in these two crystals [refer to Figs. 2(c) and (d)].

The electrical transport properties were measured to establish whether the magnetism and electrical conductivity were possibly correlated. Figure 2(e) shows the temperature dependence of the resistivity measured for the $CaFeO_3$ single crystal. Owing to the well-known CD, a metal-to-insulator transition occurs at $T_{CD} \approx 290$ K. Below the $T_{CD}$ of $CaFeO_3$, the resistivity monotonously increases upon cooling without discernible anomalies at the two AFM transition temperatures $T_{N1}$ and $T_{N2}$. Figure 2(f) shows the resistivity as a function of temperature for the $CaFe_{0.95}Co_{0.05}O_3$ crystal. Co doping of only 5% sharply lowers the $T_{CD}$ to approximately 260 K. Above this temperature, the crystal exhibits metallic electrical transport behavior owing to the presence of $Fe^{4+}/Co^{4+}$ charge states with strong $p-d$ hybridization. However, below the $T_{CD}$, the resistivity starts to increase with decreasing temperature. This electrically insulating feature confirms the occurrence of CD between the $Fe^{3+}$ and $Fe^{5+}$ states. Moreover, the remarkable decrease in $T_{CD}$ from $CaFeO_3$ to $CaFe_{0.95}Co_{0.05}O_3$ suggests the absence of crystal phase separation in the latter (*i.e.*, 95% $CaFeO_3$ + 5% $CaCoO_3$ in nominal [21,24]), or the major $CaFeO_3$ component will cause a sharp increase in resistivity at $T_{CD} \sim 290$ K. Therefore, the doped Co ions are homogeneously solute with the B-site Fe ions, consistent with the EDS mapping results. Although the two AFM transitions are not accompanied by any visible anomaly in the resistivity of $CaFeO_3$, the resistivity curve of $CaFe_{0.95}Co_{0.05}O_3$ exhibits a clear kink at $T_{N2}$. More interestingly, as the temperature decreases to $T_{N3}$, the magnitude of resistivity sharply decreases, suggesting that the

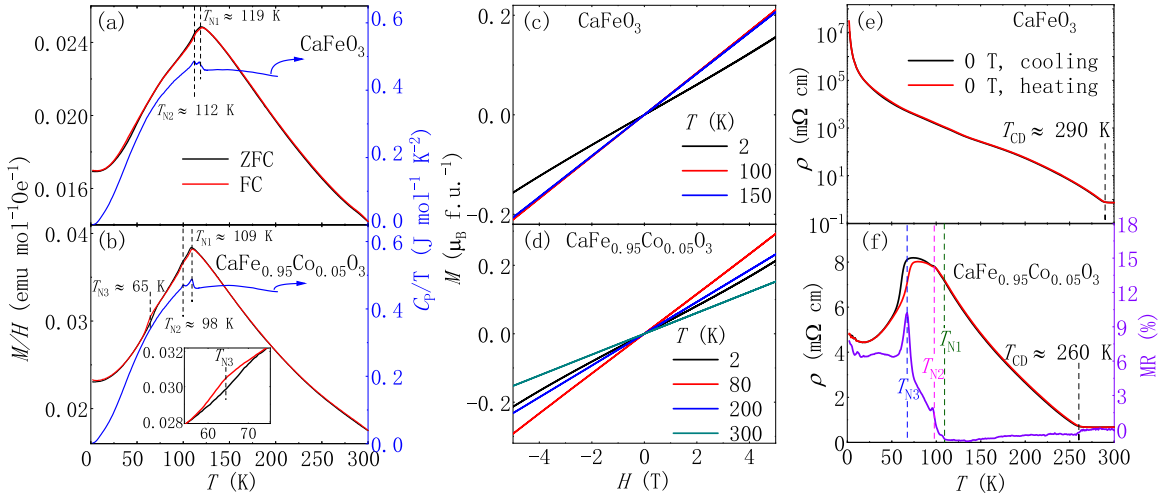


FIG. 2. Magnetic and electrical properties for $CaFeO_3$ and $CaFe_{0.95}Co_{0.05}O_3$ single crystals (at random plane). (a), (b) Temperature dependence of magnetic susceptibility measured at 0.1 T and specific heat measured at zero field for $CaFeO_3$ and $CaFe_{0.95}Co_{0.05}O_3$, respectively. The inset in (b) shows an enlarged view of the newly presented third magnetic transition at $T_{N3}$. Magnetic field dependence of magnetization for (c) $CaFeO_3$, and (d) $CaFe_{0.95}Co_{0.05}O_3$ single crystals at different temperatures. (e), (f) Temperature dependence of resistivity measured at zero field during both heating and cooling processes for $CaFeO_3$ and $CaFe_{0.95}Co_{0.05}O_3$, respectively. Temperature-dependent magnetoresistance calculated using the function MR (%) = 100%×[$\rho$(7 T) − $\rho$(0 T)]/$\rho$(0 T) is also shown in (f) based on the resistivity curves measured at 0 and 7 T for $CaFe_{0.95}Co_{0.05}O_3$.

$CaFe_{0.95}Co_{0.05}O_3$ single crystal undergoes a new transition to a low-resistance state below $T_{N3}$. In coherence with the magnetic susceptibility, the resistivity in the vicinity of $T_{N3}$ also exhibits thermal hysteresis. Furthermore, the application of a 7 T field while measuring the resistivity to calculate the magnetoresistance (MR) effect for $CaFe_{0.95}Co_{0.05}O_3$ indicates that the magnetic field plays an important role in electrical transport. As shown in Fig. 2(f), an MR peak occurs at $T_{N3}$ with a positive value of up to 10.2%. In addition to the drastic MR anomalies at $T_{N2}$ and $T_{N3}$, small MR variations appear at $T_{N1}$ and even $T_{CD}$, confirming the strong magnetic and electrical correlations in the Co-doped $CaFe_{0.95}Co_{0.05}O_3$ single crystal. This is essentially different from that observed in $CaFeO_3$ crystal without chemical doping.

$^{57}$Fe Mössbauer spectra of the $CaFe_{0.95}Co_{0.05}O_3$ powder sample were recorded at different temperatures to determine whether the charge-disproportionated $Fe^{3+}$ and $Fe^{5+}$ states reverted to the charge-unified $Fe^{4+}$ state so as to lead to the new low-resistance state below $T_{N3}$. As shown in Fig. 3(a) and Table II, the Mössbauer spectrum acquired at 292 K ($>T_{CD}$) could be well fitted based on a singlet Fe ionic state. The fitting generated a 0.045 mm s$^{-1}$ isomer shift and a naught hyperfine field, suggesting a unified and nonmagnetic $Fe^{4+}$ state. In contrast, below $T_{CD}$, the spectra were separated into two different components. In particular, at 25 K and 4 K, two sextuplet fittings comprising the $Fe^{3+}$ and $Fe^{5+}$ ionic states in a 1:1 ratio were able to reproduce the recorded spectra well, providing convincing evidence for the maintenance of CD below $T_{N3}$. The substitution of Co for Fe disturbs the magnetic ordering in $CaFe_{0.95}Co_{0.05}O_3$, leading to an inner-side broadening of the magnetically split peaks at 100 K, close to the $T_{N1}$. Therefore, simple fitting with a Lorentzian for the Mössbauer spectrum measured at 100 K resulted in some deviations. However, the spectrum could be roughly reproduced by two sextets with distinct large and small hyperfine fields, which correspond to the charge-disproportionated $Fe^{3+}$ and $Fe^{5+}$ states. In fact, in all $Fe^{4+}$-based compounds with CD, the CD is robust upon cooling [1,25]. Moreover, based on powder neutron diffraction, the $CaFe_{0.95}Co_{0.05}O_3$ possesses a charge-disproportionated $P2_1/n$ crystal structure below $T_{CD}$. As an example, the detailed refinement results for the powder neutron diffraction pattern collected at 4 K are shown in Fig. 4 and Table III.

TABLE II. Mossbauer parameters of $CaFe_{0.95}Co_{0.05}O_3$ fitted at 292, 100, 25, and 4 K.

| $T$ (K) | Component | Isomer shift (mms$^{-1}$) | Hyperfine field (kOe) | Quadrupole splitting (mms$^{-1}$) | FWHM (mms$^{-1}$) | Area (%) |
|---|---|---|---|---|---|---|
| 292 | $Fe^{4+}$ | 0.045 | 0 | 0.31 | 0.82 | 100 |
| 100 | $Fe^{3+}$ | 0.36 | 240 | 0 | ave. 0.65 | 50 |
| | $Fe^{5+}$ | −0.08 | 159 | 0 | ave. 0.60 | 50 |
| 25 | $Fe^{3+}$ | 0.294 | 400 | 0 | ave. 0.41 | 50.4 |
| | $Fe^{5+}$ | −0.002 | 277.1 | 0 | ave. 0.41 | 49.6 |
| 4 | $Fe^{3+}$ | 0.293 | 407 | 0 | ave. 0.41 | 50.6 |
| | $Fe^{5+}$ | −0.004 | 282.8 | 0 | ave. 0.41 | 49.4 |

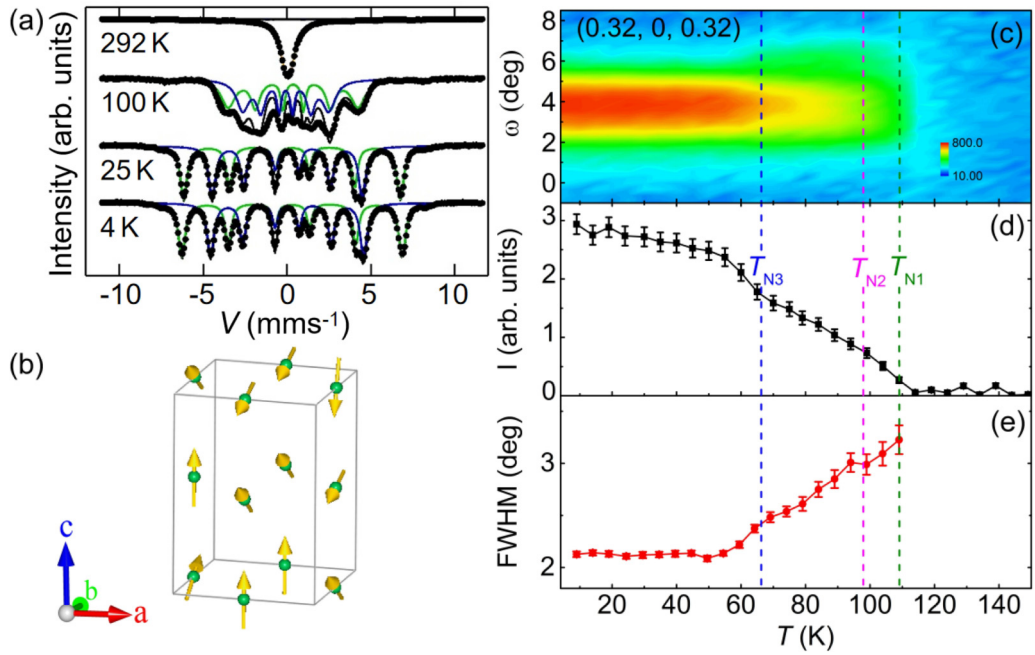


FIG. 3. Charge and spin state variations for $CaFe_{0.95}Co_{0.05}O_3$ single crystal. (a) $^{57}$Fe Mössbauer spectra for powdered sample recorded at different temperatures. The dots show the experimental data, and the orange, green, and blue curves represent the fitted $Fe^{4+}$, $Fe^{3+}$, and $Fe^{5+}$ spectrum, respectively, and the black curve is their sum. (b) Schematic spiral AFM structure with the propagation vector along the pseudocubic [111] direction. (c) Temperature dependence of the order parameter measured at the magnetic Bragg peak (0.32, 0, 0.32). (d), (e) Integrated intensity and full width at half maximum (FWHM) derived from the contour plot of the rocking curve scan in (c), respectively.

TABLE III. Refinement structure parameters of $CaFe_{0.95}Co_{0.05}O_3$ obtained at 4 K from powder neutron diffraction. Space group: $P2_1/n$, atomic positions: Ca 4*e* (*x*, *y*, *z*), Fe1/Co1 2*a* (0.5, 0, 0), Fe2/Co2 2*b* (0, 0.5, 0), O1, O2 and O3 4*e* (*x*, *y*, *z*).

| Parameters | Value |
|---|---|
| a (Å) | 5.30755(15) |
| b (Å) | 5.34364(14) |
| c (Å) | 7.51507(21) |
| $\beta$ (deg) | 89.963(7) |
| Ca1 (*x*) (Å) | 0.0057(9) |
| Ca1 (*y*) (Å) | 0.0366(4) |
| Ca1 (*z*) (Å) | 0.755(2) |
| O1 (*x*) (Å) | 0.718(2) |
| O1 (*y*) (Å) | 0.295(1) |
| O1 (*z*) (Å) | 0.961(9) |
| O2 (*x*) (Å) | 0.713(2) |
| O2 (*y*) (Å) | 0.282(2) |
| O2 (*z*) (Å) | 0.529(8) |
| O3 (*x*) (Å) | 0.069(6) |
| O3 (*y*) (Å) | 0.491(5) |
| O3 (*z*) (Å) | 0.752(9) |
| Fe1/Co1-O1 (Å) | 1.979(8) |
| Fe1/Co1-O2 (Å) | 1.933(8) |
| Fe1/Co1-O3 (Å) | 1.932(7) |
| Fe2/Co2-O1 (Å) | 1.877(9) |
| Fe2/Co2-O2 (Å) | 1.894(8) |
| Fe2/Co2-O3 (Å) | 1.898(7) |
| ∠Fe1/Co1-O1-Fe2/Co2 (deg) | 155.2(4) |
| ∠Fe1/Co1-O2-Fe2/Co2 (deg) | 159.5(3) |
| ∠Fe1/Co1-O3-Fe2/Co2 (deg) | 157.8(3) |

Single-crystal neutron diffraction was also performed on $CaFe_{0.95}Co_{0.05}O_3$ crystal at selected temperatures to track the different magnetic orders. Similar to the parent compound $CaFeO_3$, a proper-screw AFM structure with a spin moment lying in the (111) plane was observed in the doped $CaFe_{0.95}Co_{0.05}O_3$ [refer to Fig. 3(b)]. The propagation

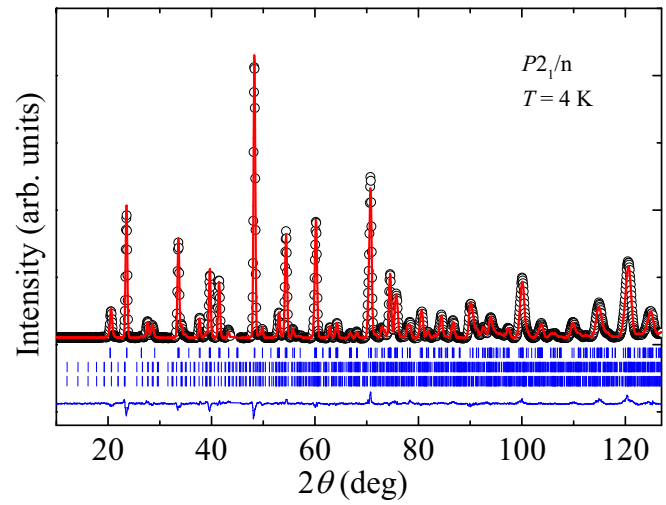


FIG. 4. Powder neutron diffraction pattern and refinement results for $CaFe_{0.95}Co_{0.05}O_3$ at 4 K. The observed (circles), calculated (red line), and difference (blue line) patterns are shown. The first-line ticks show the positions of the nuclear Bragg reflections with space group $P2_1/n$, suggesting a $Fe^{3+}$ and $Fe^{5+}$ charge-disproportionated state. The second- and third-line ticks show the reflections from the spiral antiferromagnetic spin structure.

vectors we obtained are (0.32, 0, 0.32), indicating a clear incommensurate spiral AFM spin structure. Although the magnetic susceptibility and resistivity measurements undergo significant variations at the three AFM temperatures, the single-crystal neutron diffraction was unable to differentiate the changes in the spin structure at $T_{N2}$ and $T_{N3}$ from that stabilized below $T_{N1}$, probably because of the effect of crystal twins. However, the order parameter of $CaFe_{0.95}Co_{0.05}O_3$ measured at the magnetic Bragg peak (0.32, 0, 0.32) shows two successive transitions at $T_{N1}$ and $T_{N3}$ [Figs. 3(c) and 3(d)]. Plotting the full width at half maximum (FWHM) of this magnetic Bragg peak as a function of temperature can reveal an additional anomaly at $T_{N2}$ [see Fig. 3(e)]. The additional increase in magnetic Bragg peak intensity below $T_{N3}$ [Fig. 3(d)] is attributed to the enhancement of AFM spin correlations and the stabilization of long-range magnetic order, as evidenced by the saturation of the FWHM at this temperature [Fig. 3(e)], indicating that the spiral spin structure becomes fully established.

Several lines of evidence support that the anomaly at $T_{N3}$ represents a magnetic phase transition rather than merely a secondary effect of the electrical transition. First, the thermal hysteresis between ZFC and FC curves indicates a first-order-like magnetic transition, distinct from the second-order transitions at $T_{N1}$ and $T_{N2}$. Second, single-crystal neutron diffraction reveals that the full width at half maximum (FWHM) of the magnetic Bragg peak (0.32, 0, 0.32) stabilizes below $T_{N3}$ [Fig. 3(e)], indicating a change in magnetic correlation length or spin configuration. Third, the magnetoresistance peaks precisely at $T_{N3}$ [Fig. 2(f)], demonstrating strong spin-charge coupling. We suggest that the relatively weak susceptibility anomaly at $T_{N3}$ may reflect a reorientation or modulation of the spiral spin structure (such as a change in the cone angle or ellipticity) rather than a major change in the ordered moment magnitude, which is why the neutron order parameter shows gradual saturation rather than a sharp jump.

To gain deeper insight into the unexpected magnetic and electrical transitions in the charge-disproportionated phase of $CaFe_{0.95}Co_{0.05}O_3$ single crystal occurring at $T_{N3}$, first-principles calculations were performed based on density functional theory by considering the onsite Coulomb interactions of 3*d* electrons. As reported elsewhere [6], for the parent compound $CaFeO_3$, our calculations can well reproduce the $Fe^{3+}$ and $Fe^{5+}$ charge-disproportionated insulating state with a finite energy gap (see Supplemental Material Figure S1 [23]). To simulate the effect of the low Co concentration of $CaFeO_3$, we constructed a supercell comprising 12 formula units and used the special composition $Ca_{12}Fe_{11}Co_1O_{36}$ by replacing one of the $Fe^{3+}$ or $Fe^{5+}$ ions with Co to study the ground-state properties. Note that it is difficult to lower the amount of doping, as the calculations are already time-consuming for such a large supercell with 60 atoms. In addition, because the spiral spin structure involves too many atoms to effectively calculate, the collinear ferromagnetic (FM) and A-type, C-type, and G-type AFM structures were considered for comparison. Therefore, our calculations should be regarded as an illustration of the principle. In all cases, the $Fe^{3+}$ and $Fe^{5+}$ CD were not affected by the low Co dopant concentration.

DFT calculations indicate that Co preferentially substitutes the $Fe^{5+}$ sites in both FM and A-AFM configurations (see Supplemental Material Table S1, Section S2 [23]), with an energy gain of approximately 47 meV/f.u. for the A-AFM order (closest to the experimental spiral structure). This preference may originate from the ionic radius matching between $Co^{4+}$ (intermediate spin, ~0.56 Å) and $Fe^{5+}$ (low spin, ~0.49 Å) compared to $Fe^{3+}$ (high spin, ~0.645 Å). Among all the magnetic configurations, the FM structure is energetically the most favorable but, in terms of its energy, only differs from that of the A-type AFM configuration by approximately 18 meV/f.u. (see Supplemental Material Table S2, Sec. S3 [23]). In the lowest-energy FM configuration, the nearest-neighboring spins are ferromagnetically coupled. For the A-type configuration, there is FM in-plane coupling and AFM out-of-plane coupling for the nearest neighbors. This was also observed in the spiral AFM structure from the neutron diffraction results.

The electronic band structures for both the FM and A-type AFM configurations are plotted in Fig. 5 for comparison (see Supplemental Material Figure S2 for the density of states [23]). The FM configuration has a finite energy gap in both the spin-up and spin-down channels regardless of whether Co resides at either the $Fe^{3+}$ or $Fe^{5+}$ sites, whereas the A-type AFM structure becomes metallic, particularly when Co occupies the $Fe^{3+}$ site, suggesting that the AFM structure favors metallic behavior. Considering the fact of high-spin $Fe^{4+}$ and intermediate-spin $Co^{4+}$, as confirmed in the analogous $SrFeO_3$ and $SrCoO_3$ [4,13,26], the replacement of Fe by Co introduces one additional $t_{2g}$ electron with opposite spin orientation. Therefore, the motion of the additional electrons introduced by using a small amount of Co as a dopant would be expected to be effectively blocked in the FM state because of the finite spin gap, and the system would remain insulating. In contrast, in an AFM environment, such a spin blockade does not occur, and the additional electrons can hop, causing metallic-like transport behavior. This can be demonstrated by calculating the band structures for the A-type AFM, where the spins are assumed for simplicity to align ferromagnetically within the *ab* plane, but antiferromagnetically along the *c*-axis. As shown in Fig. 5 (on the right), some bands cross the Fermi level along the F-Q and Z-G directions ($k_z$), revealing that the additional 3*d*-electrons can move along the assumed AFM alignment direction.

In the experiment, $CaFe_{0.95}Co_{0.05}O_3$ exhibits a spiral AFM structure, which contains a moderate spin rotation between the neighboring FM planes. As a result, the spin blockade effect is expected to be partially relieved in the spiral phase, and the system may even become metallic-like if the rotation is not too small. Therefore, we suggest that Co doping could lead to conducting filaments formed by neighboring dopant ions along the direction of the AFM propagation vector. Although the CD could be reduced along the conducting paths, the remaining $Fe^{3+}$ and $Fe^{5+}$ lattices would be protected by the in-plane FM order, thereby maintaining the CD even in the state with reduced resistivity. Therefore, a state with reduced resistivity is realized within the charge-disproportionated framework in $CaFe_{0.95}Co_{0.05}O_3$ single crystal, through its coupling with the peculiar spiral magnetism. Note that the actual spiral AFM structure observed experimentally, with its gradual spin

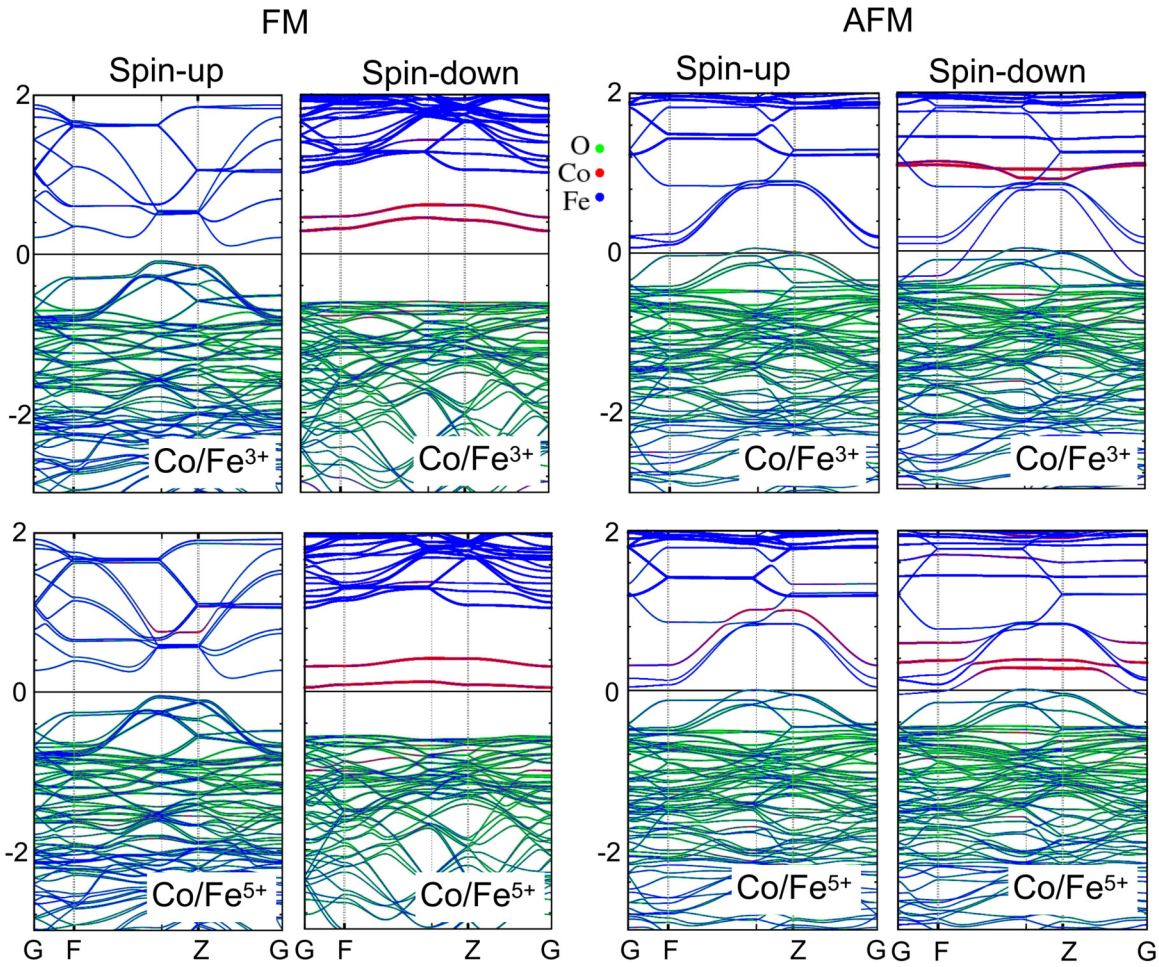


FIG. 5. First-principles band structures of $Ca_{12}Fe_{11}Co_1O_{36}$ for both FM and A-type AFM configurations with Co occupying either the $Fe^{3+}$ ($Co/Fe^{3+}$) or $Fe^{5+}$ ($Co/Fe^{5+}$) site. The $k_x$ direction is almost identical to the $k_y$ direction in the original Brillouin zone and therefore not shown in the band plot. For the spiral AFM and lower doping concentrations, the energy gap along the ferromagnetic ($k_x$, $k_y$) plane will increase towards that of the FM configuration.

rotation between FM-coupled planes, is expected to exhibit electronic properties interpolating between the FM (insulating) and A-type AFM (metallic) configurations calculated here. As the spin canting angle decreases from 180° (A-type) toward 0° (FM), the spin blockade is gradually lifted, allowing the additional $t_{2g}$ electrons from Co to hop along the propagation vector direction. Furthermore, we acknowledge that the supercell used (corresponding to ∼8.33% Co doping) slightly overestimates the dopant concentration compared to the experimental 5%, and the periodic boundary conditions may artificially enhance inter-dopant interactions. Nevertheless, this model provides a qualitatively correct picture of the local electronic structure modifications induced by Co doping.

## IV. CONCLUSIONS

In conclusion, stoichiometric $CaFeO_3$ and $CaFe_{0.95}Co_{0.05}O_3$ single crystals were prepared by combining the floating-zone technique with subsequent high-pressure oxygen treatment. The introduction of a low concentration (5%) of Co at the B-site can sharply decrease the $T_{CD}$ to 260 K, where a metal-to-insulator transition occurs because of the disproportionated $Fe^{3+}$ and $Fe^{5+}$ states. Upon further cooling to $T_{N1} \approx 109$ K and $T_{N2} \approx 98$ K, $CaFe_{0.95}Co_{0.05}O_3$ experienced double AFM transitions with apparent anomalies in resistivity and/or MR. To our surprise, as the temperature decreased to $T_{N3} \approx 65$ K, a third AFM phase transition, which was never observed in the parent $CaFeO_3$, occurred. Moreover, an unexpected electrical transition with a drastic decrease in resistivity takes place, accompanied by the newly presented AFM transition at $T_{N3}$ in $CaFe_{0.95}Co_{0.05}O_3$, although the $Fe^{3+}$ and $Fe^{5+}$ charge-disproportionated states exist robustly at low temperatures. First-principles calculations indicate that the occupancy of the $Fe^{3+}$ sites by Co plays a more critical role in the metallic state within the charge-disproportionated framework, most probably by producing conducting filaments along the direction of the AFM propagation vector against the background of the $Fe^{3+}$- and $Fe^{5+}$-ordered lattices. This study opens a way to realize new electronic states within the charge-disproportionated framework by delicate chemical doping.

## ACKNOWLEDGMENTS

This work was supported by the National Key R&D Program of China (Grant No. 2021YFA1400300) and the

National Natural Science Foundation of China (Grant No. 12425403). Research conducted at ORNL's High Flux Isotope Reactor was sponsored by the Scientific User Facilities Division, Office of Basic Energy Sciences, US Department of Energy.

H.X., Z.L., and Y.W. contributed equally to this work.

## DATA AVAILABILITY

The data that support the findings of this article are not publicly available because they contain commercially sensitive information. The data are available from the authors upon reasonable request.

[1] P. M. Woodward, D. E. Cox, E. Moshopoulou, A. W. Sleight, and S. Morimoto, Structural studies of charge disproportionation and magnetic order in $CaFeO_3$, Phys. Rev. B **62**, 844 (2000).

[2] S. Ishiwata, M. Tokunaga, Y. Kaneko, D. Okuyama, Y. Tokunaga, S. Wakimoto, K. Kakurai, T. Arima, Y. Taguchi, and Y. Tokura, Versatile helimagnetic phases under magnetic fields in cubic perovskite $SrFeO_3$, Phys. Rev. B **84**, 054427 (2011).

[3] Y. Liu, Z. Liu, Z. Li, S. Qin, X. Ye, X. Shen, B. Zhou, G. Zhou, S. Agrestini, M. Valvidares, H. B. Vasili, Z. Hu, and Y. Long, Multiple magnetic transitions and electrical transport transformation of a $BaFeO_3$ cubic perovskite single crystal, Phys. Rev. B **101**, 144421 (2020).

[4] Y. Long, Y. Kaneko, S. Ishiwata, Y. Taguchi, and Y. Tokura, Synthesis of cubic $SrCoO_3$ single crystal and its anisotropic magnetic and transport properties, J. Phys.: Condens. Matter **23**, 245601 (2011).

[5] H. Wang, J. Yang, C. Dong, Q. Mao, J. Du, and M. Fang, Crystal growth and characterization of the quasi-one-dimensional compound $BaCoO_3$, J. Cryst. Growth **430**, 52 (2015).

[6] J. B. Yang, M. S. Kim, Q. Cai, X. D. Zhou, H. U. Anderson, W. J. James, and W. B. Yelon, Study of the electronic structure of $CaFeO_3$, J. Appl. Phys. **97**, 10A312 (2005).

[7] Q. Sun and Z. Yang, The charge disproportionation and electric properties of perovskite $CaFe_{1-x}Co_xO_3$, Results Phys. **24**, 104198 (2021).

[8] L. Jiang, D. Saldana-Greco, J. T. Schick, and A. M. Rappe, Enhanced charge ordering transition in doped $CaFeO_3$ through steric templating, Phys. Rev. B **89**, 235106 (2014).

[9] H. Zhang, H. Shi, H. You, M. Su, L. Huang, Z. Zhou, C. Zhang, J. Zuo, J. Yan, and T. Xiao, Cu-doped $CaFeO_3$ perovskite oxide as oxygen reduction catalyst in air cathode microbial fuel cells, Environ. Res. **214**, 113968 (2022).

[10] H. A. Alyousef, S. A. M. Abdelmohsen, A. S. Alqarny, N. Alotaibi, Y. Ejaz, M. Imran, and H. M. Farid, Specifying the Mo doped $CaFeO_3$ electrode material for the application in supercapacitor, Appl. Phys. A **131**, 382 (2025).

[11] S. Kawasaki, M. Takano, and Y. Takeda, Physical properties of Co-substituted iron perovskite systems, Solid State Ionics **108**, 221 (1998).

[12] M. Azuma, T. Saito, S. Ishiwata, I. Yamada, Y. Kohsaka, H. Takagi, and M. Takano, Single crystal growth of transition metal oxides at high pressures of several GPa, Physica C **392–396**, 22 (2003).

[13] Y. W. Long, Y. Kaneko, S. Ishiwata, Y. Tokunaga, T. Matsuda, H. Wadati, Y. Tanaka, S. Shin, Y. Tokura, and Y. Taguchi, Evolution of magnetic phases in single crystals of $SrFe_{1-x}Co_xO_3$ solid solution, Phys. Rev. B **86**, 064436 (2012).

[14] S. Qin, B. Zhou, Z. Liu, X. Ye, X. Zhang, Z. Pan, and Y. Long, Slight Co-doping tuned magnetic and electric properties on cubic $BaFeO_3$ single crystal, Chin Phys. B **31**, 097503 (2022).

[15] J. Fujioka, S. Ishiwata, Y. Kaneko, Y. Taguchi, and Y. Tokura, Variation of charge dynamics upon the helimagnetic and metal-insulator transitions for perovskite $AFeO_3$ ($A$ = Sr and Ca), Phys. Rev. B **85**, 155141 (2012).

[16] S. Ishiwata, M. Azuma, T. Saito, S. Kawasaki, and M. Takano, Single crystal growth of $CaFeO_3$ at high pressure, J. Jpn. Soc. Powder and Powder Metallurgy **48**, 715 (2001).

[17] H. L. Xia, Y. Y. Yin, J. H. Dai, J. Y. Yang, X. M. Qin, C. Q. Jin, and Y. W. Long, Magnetism and magnetocaloric effect study of $CaFe_{0.7}Co_{0.3}O_3$, Mater. Res. Express **2**, 046103 (2015).

[18] B. C. Chakoumakos, H. Cao, F. Ye, A. D. Stoica, M. Popovici, M. Sundaram, W. Zhou, J. S. Hicks, G. W. Lynn, and R. A. Riedel, Four-circle single-crystal neutron diffractometer at the high flux isotope reactor, J. Appl. Crystallogr. **44**, 655 (2011).

[19] J. Rodríguez-Carvajal, Recent advances in magnetic structure determination by neutron powder diffraction, Physica B **192**, 55 (1993).

[20] P. Blaha, K. Schwarz, G. K. H. Madsen, D. Kvasnicka, and J. Luitz, *WIEN2k: An Augmented Plane Wave + Local Orbitals Program for Calculating Crystal Properties* (Karlheinz Schwarz, Technische Universitat Wien, Wien, Austria, 2013).

[21] H. Xia, J. Dai, Y. Xu, Y. Yin, X. Wang, Z. Liu, M. Liu, M. A. McGuire, X. Li, Z. Li, C. Jin, Y. Yang, J. Zhou, and Y. Long, Magnetism and the spin state in cubic perovskite $CaCoO_3$ synthesized under high pressure, Phys. Rev. Mater. **1**, 024406 (2017).

[22] T. Saha-Dasgupta, Z. S. Popović, and S. Satpathy, Density functional study of the insulating ground states in $CaFeO_3$ and $La_{1/3}Sr_{2/3}FeO_3$ compounds, Phys. Rev. B **72**, 045143 (2005).

[23] See Supplemental Material at http://link.aps.org/supplemental/10.1103/lssr-fzlr for additional computational details, including Hubbard U parameter tests, Co substitution site preference analysis, magnetic configuration energy comparisons, and density of states calculations.

[24] T. Osaka, H. Takahashi, H. Sagayama, Y. Yamasaki, and S. Ishiwata, High-pressure synthesis of an unusual antiferromagnetic metal $CaCoO_3$ with $GdFeO_3$-type perovskite structure, Phys. Rev. B **95**, 224440 (2017).

[25] Y. Shimakawa, Crystal and magnetic structures of $CaCu_3Fe_4O_{12}$ and $LaCu_3Fe_4O_{12}$: Distinct charge transitions of unusual high valence Fe, J. Phys. D Appl. Phys. **48**, 504006 (2015).

[26] M. Reehuis, C. Ulrich, A. Maljuk, C. Niedermayer, B. Ouladdiaf, A. Hoser, T. Hofmann, and B. Keimer, Neutron diffraction study of spin and charge ordering in $SrFeO_{3-\delta}$, Phys. Rev. B **85**, 184109 (2012).